Additive Manufacturing 37 (2021) 101703

Contents lists available at ScienceDirect

Additive Manufacturing

journal homepage: www.elsevier.com/locate/addma

Research Paper

Digital metal printing by electrohydrodynamic ejection and in-flight melting of microparticles

Henry Merrow [a], Justin D. Beroz [a,b], Kaihao Zhang [a], Ulrich P. Muecke [a,c], A. John Hart [a,*]

[a] Department of Mechanical Engineering, Massachusetts Institute of Technology, Cambridge, MA 02139, USA
[b] Department of Physics, Massachusetts Institute of Technology, Cambridge, MA 02139, USA
[c] Department of Materials Science and Engineering, Massachusetts Institute of Technology, Cambridge, MA 02139, USA

ARTICLE INFO

Keywords:
Laser
Electrohydrodynamic
Melting
Droplet
Solidification

ABSTRACT

Metal additive manufacturing (AM) will impact many industries, including those producting of advanced structural, propulsion, electronic, and thermal systems. Many established metal AM processes involve layer-by-layer deposition and selective binding or melting of metal powders. However, these processes do not easily permit multi-material printing or printing directly onto non-planar surfaces. By contrast, AM techniques that deposit metal directly are typically low resolution (e.g., directed energy deposition), or cannot achieve bulk metal properties (e.g., ink-based methods). Here, we present a high resolution direct metal printing method that potentially addresses these limitations. Individual metal microparticles are electrohydrodynamically ejected on-demand from a nozzle-confined meniscus and laser-melted in-flight before landing and solidifying on a substrate. We demonstrate printing of solder and platinum particles ranging in size from 30 to 150 μm and explore the process parameter space as limited by the ejection conditions and the kinetics of melting, impact, and solidification. Our experiments demonstrate process compatibility with a wide range of powder feedstock materials, and tunability of the solidified morphology via the laser processing parameters.

1. Introduction

Additive manufacturing (AM), which encompasses many process technologies for polymers, metals, composites, and other materials, enables on-demand component production with increased geometric complexity compared to conventional manufacturing technologies. AM therefore is attractive for many applications, including lightweight components for aircraft and automobiles, customized medical implants, high-performance mold tooling, and load-bearing devices such as housings with embedded heat exchangers or electrical interconnects [1,2]. Metal AM in particular is well suited to provide value for industrial applications given the ability to print complex functional and structural parts with fine features.

The most widely used metal AM methods to-date are laser powder bed fusion (here referred to as selective laser melting, SLM), binder jetting (BJ), and directed energy deposition (DED). With SLM and BJ, parts are fabricated layer-by-layer via powder-bed processes. In SLM, a scanned laser beam selectively melts the desired pattern in each powder layer [3]. In BJ, an inkjet printhead is used to deposit a binding agent to form the desired pattern in each powder layer, and after all the layers have been printed, the binder is cured and the part is sintered in a furnace [4]. With DED, a powder or wire is fed from a nozzle towards the part and is melted as it approaches and contacts the part such that it can fuse to the material that has already been deposited. The relative position and orientation of the build platform and/or the print nozzle are controlled to build up the desired 3D shape layer-by-layer [5]. For all these technologies, there is a tradeoff between throughput and resolution; i.e. higher throughput may be achieved at the cost of lower resolution and part quality. Moreover, high-resolution, multi-material printing of arbitrary metals into monolithic components is not achievable by any current process.

High-resolution AM of metallic materials is desirable for many applications, including printing of electrical elements, e.g., interconnects, inductors, antennas, onto and within existing components and housings. Ink-based methods, employing inks loaded with metal nanoparticles, are one approach for depositing metal onto substrates to build up 2D features and 3D parts. Inkjet methods involve jetting of discrete nanoparticle-loaded droplets followed by evaporation of the liquid and sintering of the nanoparticles. This allows for high resolution printing, with layer thicknesses typically hundreds of nanometers and line widths

* Corresponding author.
E-mail address: ajhart@mit.edu (A.J. Hart).

https://doi.org/10.1016/j.addma.2020.101703
Received 13 August 2020; Received in revised form 12 October 2020; Accepted 7 November 2020
Available online 13 November 2020

as small as 10–20 μm [6]. Aerosol jet printing is another ink-based method, wherein a metal nanoparticle ink is atomized to generate 1–5 μm polydisperse droplets. A carrier gas then transports the droplets to the nozzle, where an annular gas flow focuses the aerosol stream into a fine beam directed onto the substrate. With this method, 5–10 μm line widths are achievable at speeds around 200 mm s^{-1} [7]. Electrohydrodynamic (EHD) printing methods have also been employed with metal inks. In this case an electric potential is applied between the print nozzle (filled with ink) and a bottom electrode such that a conical meniscus is formed. Typically, the flow rate of the ink and the electric potential are adjusted to form a jet from the tip of the cone. Resolution of EHD-based methods has been reported in the sub-micron range [8–10]. All of these ink-based methods enable direct metal deposition, yet achieving bulk properties of the printed features is difficult due to impurities and voids remaining after sintering of the ink particles.

For this reason, direct jetting of metals, commonly referred to as liquid metal jetting (LMJ), has been explored, both for printing of 2D features and 3D parts. Typical embodiments involve forcing a molten metal through a small orifice to generate a droplet on-demand or to generate a stream of droplets continuously. The forcing mechanism may be mechanical [11–13], pneumatic [14], or magnetohydrodynamic [15]. Continuous pneumatic jetting of aluminum (190 μm droplets) has been reported at a printing frequency of up to 24 kHz [16]. Magnetohydrodynamic methods have achieved drop-on-demand generation for droplets in the 200–300 μm size range at frequencies around 1 kHz [17]. In general, LMJ potentially offers broad material compatibility, lower-cost material feedstock, and the potential for multi-material printing [18]. However, LMJ also faces major challenges, including thermal management of a high-temperature molten metal reservoir and long-term stability of the orifice against degradation and clogging [16]. Further, management of heat accumulation during printing is also critical to maintain part accuracy and enable construction of fine features [19].

Here, we present a novel non-contact method for generating and printing molten metal droplets from a nozzle on demand, which we call digital particle ejection melting (DPEM). A microscale metal particle is introduced onto a water meniscus maintained at a needle orifice. Then, the particle is ejected via an applied electric potential between the needle and the substrate [24]. After ejection, each particle is melted in-flight by a laser beam and then lands and solidifies on the substrate. A key attribute of DPEM is that it is compatible with a wide range of materials available in particle form, including materials with very high melting points. Unlike jetting methods that require melting of the metal in a reservoir, DPEM melts the material after ejection from the nozzle, therefore not requiring the printhead to be compatible with the molten feedstock metal and making the process easily configurable for different materials. We demonstrate DPEM printing with drops as small as 30 μm diameter and show compatibility with two model materials, a lead-free solder alloy (Sn96.5-Ag3-Cu0.5) and a platinum-ruthenium alloy (Pt95.5-Ru4.5). We further demonstrate the ability to vary the printed droplet morphology by tuning the energy delivered to the particles via the laser beam, and we comment on the capabilities and limits of this technique toward an eventual 3D printing process. As exemplary printed patterns, we show a linear array of equally spaced droplets, as well as a continuous metallic line of overlapping droplets.

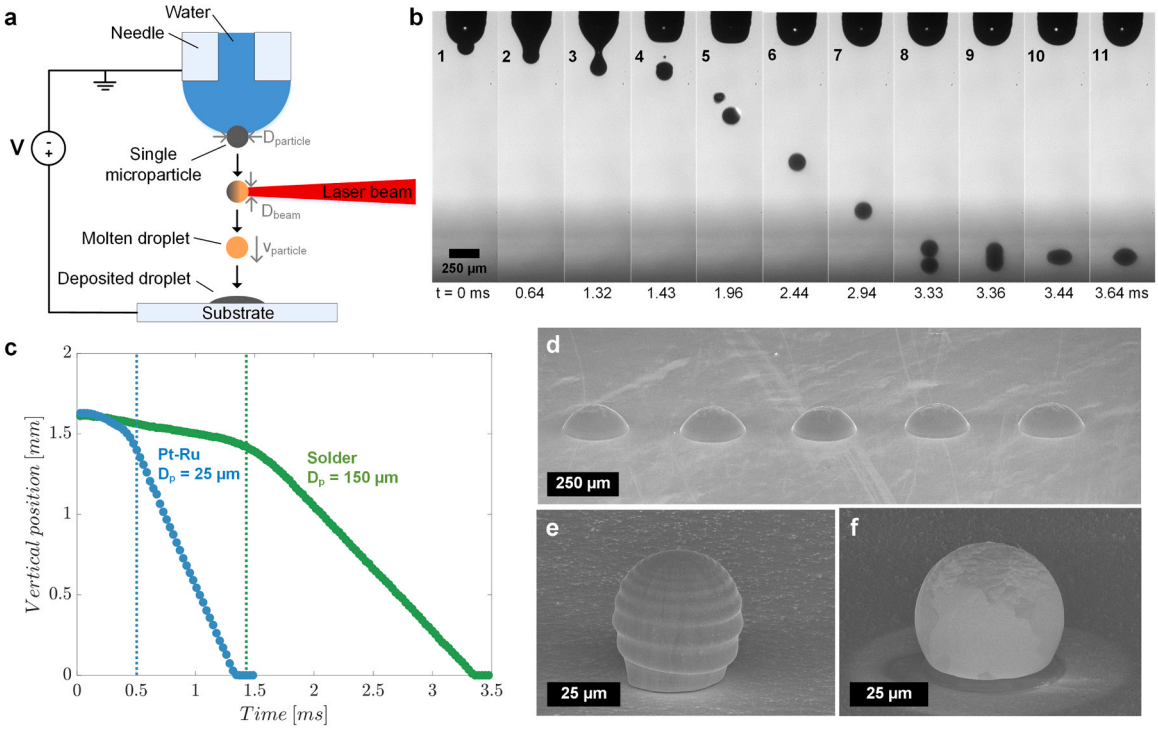

Fig. 1. Digital metal printing by electrohydrodynamic ejection and in-flight melting of microparticles. (a) Schematic illustrating the digital particle ejection and melting (DPEM) process. A solid microparticle is adsorbed on the surface of a liquid meniscus maintained at the tip of a conductive hollow needle. Applying an electric potential between the needle and the substrate deforms the meniscus such that an individual particle is ejected. A laser beam then intersects the particle, causing it to melt during flight, and the molten particle subsequently lands on the substrate and solidifies. (b) Sequential images taken from a high-speed camera showing the process of ejection, melting and deposition of a 150 μm solder particle onto a tin substrate. Images 2–4 show ejection from the meniscus. Image 5 shows the laser beam interaction and removal of a water cap that was attached to the particle. Images 8–11 show contact, spreading and solidification. (c) Plots of particle vertical position vs. time for exemplary prints of a 150 μm solder particle (green) and a 50 μm Pt-Ru particle (blue). The time corresponding to complete detachment of the particle from the meniscus is indicated by a vertical dashed line for each case. (d) Array of printed solder dots on a tin substrate. (e) Pt95.5-Ru4.5 particle printed on a Pt95.2-Ru4.8 substrate. (f) Pt95.5-Ru4.5 particle printed on a glass substrate.

2. Materials and methods

Digital printing of metal droplets is performed by first ejecting a single microparticle from a liquid meniscus and then melting the particle as it travels through a laser beam aligned perpendicularly to the particle trajectory (Fig. 1a). To achieve particle ejection, a hollow metal needle is filled with water such that a hemispherical meniscus is established at the needle orifice. A syringe connected to the needle is used to adjust the hemispherical volume of water. A single microparticle is then introduced onto the surface of the water meniscus. This is achieved by spreading particles on a platform which is then brought underneath the meniscus such that a single particle is positioned directly underneath the meniscus. The platform is then raised so that the particle contacts the meniscus and is adsorbed onto its surface (see SI). Once a particle has been loaded onto the meniscus and the particle platform has been removed, a positive voltage is applied to the conductive substrate relative to the grounded needle, typically as a pulse of 2–3 kV for a duration of 2–3 ms. The applied electric field causes the water meniscus to elongate due to the concentration of the electric field at the apex, while retaining the particle. The particle ultimately detaches with an entrained cap of liquid. Particle ejection takes place over the course of ~1 ms, depending on the size of the particle and the meniscus. The liquid used to create the meniscus should be partially wetting with respect to the particle, so that the particle may reside on the liquid meniscus before ejection without being fully engulfed. This facilitates electrohydrodynamic ejection of the particle and aides in removal of the liquid during heating of the particle by the laser. For metal particles, water has proven to function well in this regard.

While in-flight, the particle passes through a focused laser beam which melts the particle and removes the cap of liquid. The droplet then lands on the substrate, spreads and solidifies. For all experiments included here, the diameter of the needle (and thus the diameter of the water meniscus) was 360 μm, the laser beam spot size was approximately 44 μm, and the needle-substrate separation was 2.1 mm. Further details of the experimental apparatus are included in the methods and SI sections.

In Fig. 1b, we show sequential images taken from a high-speed camera during printing of a 150 μm solder particle on a polished tin substrate, indicating the deformation of the meniscus followed by particle ejection and flight toward the substrate. Here, the laser beam originates from the right side of the image. Fig. 1c shows the position of a 150 μm solder particle and a 50 μm Pt-Ru particle versus time over the course of ejection for typical prints. Fig. 1d–f show example printed droplets of solder and Pt-Ru, imaged using scanning electron microscopy (SEM). Videos of example prints of a 150 μm solder particle and a 50 μm Pt-Ru particle are included in the SI. The Pt-Ru alloy was chosen for experimentation because it has a high melting point and does not require a protective atmosphere. The solder alloy was chosen for demonstration of a common low melting point alloy.

Supplementary material related to this article can be found online at doi: 10.1016/j.addma.2020.101703.

Upon ejection, the particle typically carries a cap of liquid that forms upon detachment from the. elongated meniscus. We observe that the water cap is removed during laser heating, likely due to film boiling at the interface between the particle and the water due to the rapid heating of the particle. Film boiling creates a vapor layer between the particle and the water, and the water cap will thus detach from the particle, as seen in the fifth frame of Fig. 1b. When the cap detaches gently, the particle trajectory is not affected. However, if the particle has been fully engulfed in the meniscus before ejection, vigorous boiling throughout the volume of the water cap may occur, which can result in significant alteration of the particle trajectory. Whether or not the particle will be initially engulfed in the liquid depends primarily on the wettability of the liquid on the particle; a liquid with a low contact angle will lead to particles being more engulfed in the liquid.

3. Results

3.1. Criteria for in-flight melting of microparticles

The energy delivered to a particle in flight will determine its resulting phase (i.e. solid, liquid or partially molten) and temperature. In order to melt a metal particle, the energy delivered to the particle in-flight must be greater than the energy required to bring the particle to the melting point and undergo phase change from solid to liquid,

$$E_{delivered} \geq \rho V_p [C_s (T_{melt} - T_\infty) + \Delta H_{fusion}] \quad (1)$$

Here, ρ is the density, V_p is the particle volume, C_s is the specific heat, T_{melt} is the melting point, T_∞ is the ambient or initial temperature, and ΔH_{fusion} is the latent heat of fusion. The energy delivered to the particle is approximately as follows:

$$E_{delivered} \approx \alpha P_{laser} t_{residence} \approx \alpha P_{laser} \frac{D_p}{v_p} \quad (2)$$

Here, α is the material absorptivity, P_{laser} is the laser power, $t_{residence}$ is the residence time of the particle in the beam, D_p is the particle diameter, and v_p is the particle speed. This approximation assumes that the particle travels along the centerline of the beam spot and requires the particle diameter to be smaller than the laser beam diameter. At $\frac{D_p}{D_b} = 1.25$, the error is 10%, and at $\frac{D_p}{D_b} = 3.5$, the error is 1%, where D_b is defined as the diameter at which the beam intensity is $1/e^2 = 0.135$ times the value at its center (maximum). With the residence time and the energy delivery criterion, the power density required to melt a given particle material and size is as follows:

$$P_{laser}/V_p \geq \frac{\rho}{\alpha}[C_s (T_{melt} - T_\infty) + \Delta H_{fusion}](\frac{1}{t_{residence}}) \quad (3)$$

Minimum power densities required to melt various metals are plotted in Fig. 2a for residence times that are typical of particles that are tens to hundreds of microns in size. This analysis assumes 1064 nm laser wavelength, constant material absorptivity and heat capacity during the heating process, and no heat loss; these assumptions are appropriate for estimating system requirements but are not appropriate for precise predictions of resulting droplet temperatures (see SI). Also, calculations are given in the SI for the residence time in the general case of arbitrary particle and beam sizes.

By the above method, we predict a minimum residence time of 39 μs for melting of a 100 μm stainless steel particle (alloy 304) using a 300 W laser. Correspondingly the maximum allowable particle velocity to achieve full melting is 2.6 m s^{-1}, assuming a small beam spot size relative to the particle. Experimentally, we find that ejection speed is inversely proportional to particle size. For instance, ejection speeds of up to 3 m s^{-1} have been observed for $D_p = 30$ μm, corresponding to 10 μs residence time; speeds as slow as 0.5 m s^{-1} have been observed for $D_p = 350$ μm, corresponding to 700 μs residence time. For the data reported in Fig. 2b and c, the observed ejection speeds were between 1.0 and 1.5 m s^{-1}.

Importantly, this analysis does not consider transient heat transfer across the particle. If the timescale of heat conduction across the particle is too small relative to the residence time available to melt the particle, then overheating on the irradiated surface may occur, and metal evaporation and plasma generation are possible. This was not observed to occur for the platinum and solder alloys studied here, and thus is likely not an issue for most other alloys listed in Fig. 2a due to their higher thermal conductivity relative to platinum and solder. The exception is stainless steel, which has a thermal conductivity approximately 1/5th that of the studied alloys. However, for lower conductivity materials, it would be possible to mitigate heat conduction issues by exploring alternative optical configurations that would decrease the laser beam intensity at the surface but still achieve the same total energy input (e.g. a laser line or encircled illumination of the particle instead of a circular

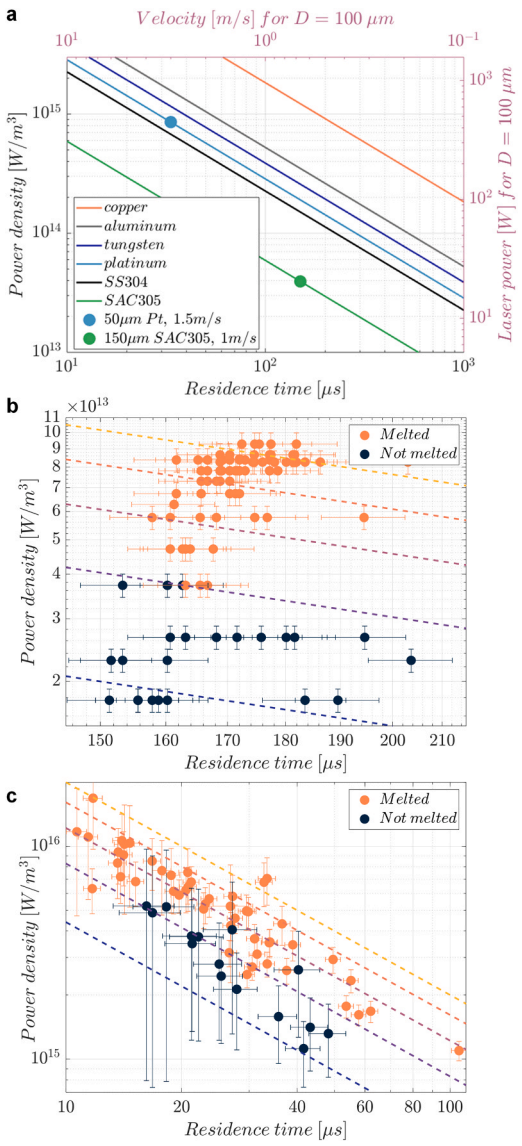

Fig. 2. Analysis of energy density required for in-flight melting of metal microparticles. (a) Estimated relationships between energy density required for melting and residence time, assuming constant absorptivity with 1064 nm laser heating. Residence time is the duration that the beam is incident on the particle during flight, and power density is normalized to the particle volume. The top horizontal axis shows the particle velocity that would correspond to the indicated residence time for a 100 μm diameter particle. The right vertical axis shows the laser power corresponding to the power density threshold for melting of a 100 μm particle. The blue and green dots represent exemplary experiment conditions, i.e. a 50 μm platinum particle printed with a velocity of 1.5 m s^{-1} and a 150 μm SAC305 particle printed with a velocity of 1.0 m s^{-1}, respectively. (b,c) Comparison of experimental results to energy density model for printing of solder (SAC305) and Pt95.5-Ru4.5 particles, respectively. Blue dots correspond to experiments during which the particle was not melted or only partially melted, and orange dots correspond to experiments during which the particle was fully melted. The dashed lines show lines of constant energy density, computed as the product of power density and residence time.

spot).

3.2. Printing of platinum and solder alloys

The necessity for a critical energy density to achieve in-flight melting is demonstrated by printing of the exemplary solder alloy (SAC305, composition Sn96.5-Ag3-Cu0.5, D_p= 150 μm, melting range 217–220 °C) and platinum alloy (Pt95.5-Ru4.5, D_p= 50–100 μm, melting range 1780–1795 °C). Data from experiments is transposed onto the axes of power density and residence time (measured from high-speed videos) in Fig. 2b and c, respectively. Orange dots correspond to cases where the particle was fully melted and blue dots correspond to cases where the particle did not fully melt. Melting was assessed by observing droplet or particle behavior upon impact with the substrate, as is described in the methods and SI sections. In spite of the simplicity of the laser heating model, the experiments confirm the validity of the critical energy density approximation to predict melting of the particle in flight. Note that the uncertainty of measurement, indicated by the error bars on each data point, is much higher for the platinum alloy because the particle size is comparable to the laser beam diameter (50–100 μm versus 44 μm, respectively). Therefore, slight misalignment between the particle trajectory and laser beam results in a significant decrease in the energy delivered to the particle (see SI).

DPEM printing also enables control of the molten metal temperature and consequently the dynamics of impact and solidification onto the printing substrate. Therefore, the amount of energy delivered to each particle and consequently the droplet temperature will result in a change in the morphology, and potentially the microstructure of the droplet on the substrate after solidification. In Fig. 3, we show images of solder droplets (SAC305, D_p= 150 μm) that were subject to different laser power settings (i.e., changing the energy density as defined above) during flight, and printed onto tin substrates. A series of SEM images (Fig. 3a) and polished and etched cross-sections (Fig. 3b) reveal how superheating influences the droplet morphology and microstructure after solidification. With increasing energy delivered, the printed metal dots have a lower aspect ratio (i.e., more spreading). In addition, the cross-section images reveal that the tin substrate was melted due to heat transfer from the impinging droplets, and the droplet and the substrate mixed before solidification.

Specifically, we define the spread factor (S) as the droplet's radius of contact with the surface divided by the initial droplet (particle) radius, R/a. We plot the spread factor versus the energy density (defined as in Eq. (2)) in Fig. 3c. For the solder, S asymptotes to 1.6 at high energy densities. Fig. 3d shows compiled results for the solidified contact angle (denoted Θ^s_∞) plotted versus energy density delivered. We attribute the increase of spread factor with increasing energy delivered primarily to lower surface tension at higher droplet temperatures [20]. This will result in a lower equilibrium contact angle along with more available time to spread before solidification pins the droplet at the interface. Previous studies of metal jetting have not reported significant sensitivity of spread factor to droplet overheating [21]. However, this had only been reported for relatively small differences in droplet temperature. In our case, the droplet temperature varies by as much as 500 °C over the range of power densities shown in Fig. 3a, resulting in both a greater change in surface tension [20] and a much longer solidification time after impact [21].

Using the parameters obtained for single-droplet printing, lines may be printed by overlapping consecutive droplets. To print exemplary lines, the nozzle was kept stationary and the substrate was moved after each droplet deposition to generate the desired pattern one particle at a time. In the example shown in Fig. 4a, the substrate (polished tin) was incrementally translated 150 μm between each print. Considering a spread factor of 1.6 and thus a maximum solidified diameter after spreading of 240 μm, the nominal droplet-to-droplet overlap is approximately 90 μm. Fig. 4b shows the cross-section of the line, indicating intimate contact between the adjacent drops. Notably, no porosity is apparent within the cross-section of the line. These observations indicate promise for achieving bulk material properties by DPEM printing.

3.3. Droplet-substrate thermal interaction and adhesion

The droplet-substrate material combination and the interface

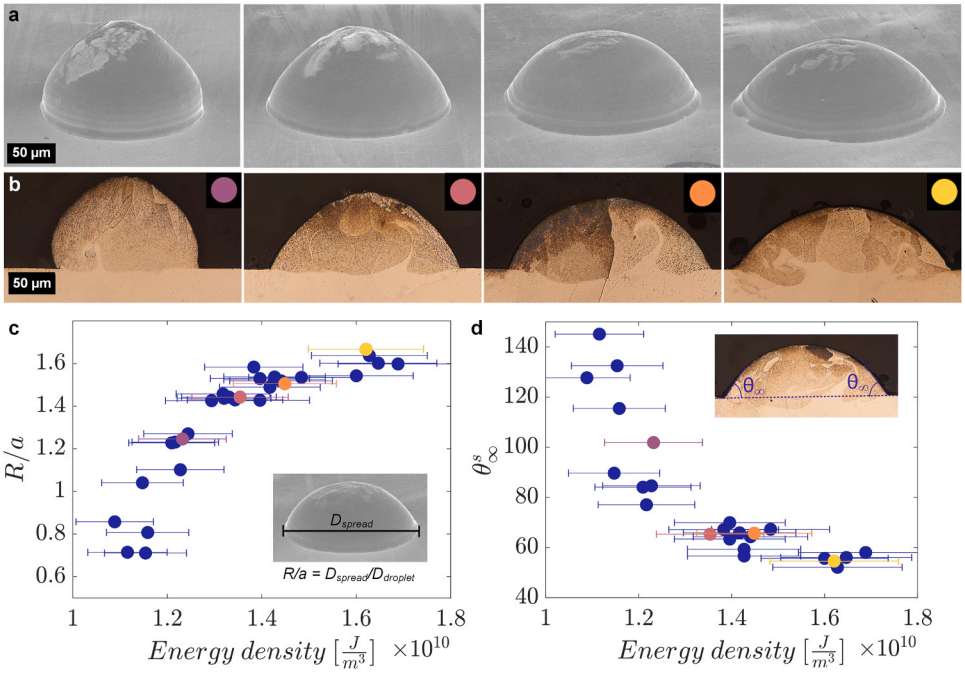

Fig. 3. Control of printed droplet morphology by energy density delivered in flight. (a) SEM images of 150 μm solder particles printed with increasing laser power (from left to right). (b) Polished and etched cross sections of the printed particles, revealing the microstructure and the interface between the particle and the substrate. (c and d) Spread factor and solidified contact angle of the printed droplets plotted versus energy density delivered, respectively. Energy density is computed as the power density (measured laser power divided by particle volume, as in Fig. 2b and c) multiplied by the residence time, where here $t_{residence} \approx \frac{D_p}{v_p}$. The dots of different colors in plots (c) and (d) correspond to the SEM images and cross-sections shown in (a) and (b).

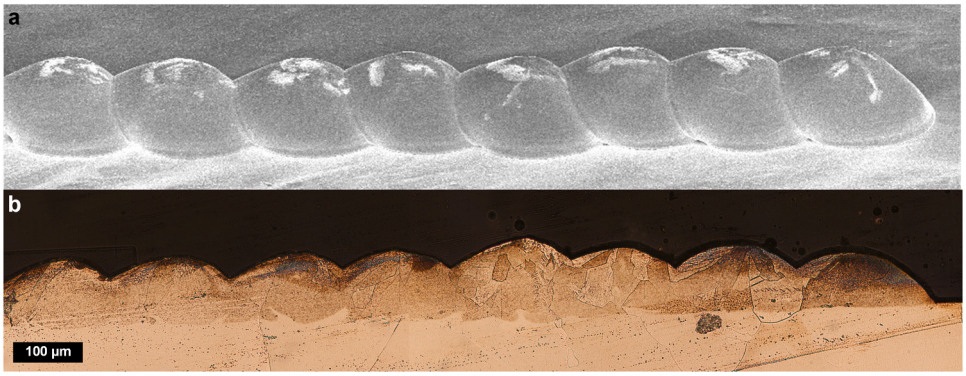

Fig. 4. Printing of overlapping droplets to form a fine metal line. (a) Line of overlapping 150 μm solder particles printed on a tin substrate. (b) Polished and etched cross-section of the printed line shown in (a). The cross-section reveals good bonding between the printed droplets and the substrate as well as between neighboring droplets; grains span lateral interfaces between, and as in Fig. 3 the cross-section indicates that the substrate was melted by the droplets.

characteristics are particularly important to droplet-substrate adhesion. Fig. 5a–e displays examples of Pt95.5-Ru4.5 particles printed on borosilicate glass, Inconel 625, and Pt95.2-Ru4.8. These substrates were chosen as examples of printing on a dielectric, a high-temperature alloy, and the same material as the particle. If the droplet remains molten during the full extent of spreading, conformal droplet-substrate contact should result. Further, if the substrate melts during droplet impact, then metallurgical bonding and strong adhesion may be possible. If the droplet does not remain molten and/or the substrate does not melt, then contact may not be conformal and adhesion may be weak. The cross-section in Fig. 5c (Inconel 625 substrate) shows that the substrate was melted and conformal contact was achieved (with relatively strong adhesion expected), while the cross-section in Fig. 5e (Pt95.2-Ru4.8 substrate) indicates that the substrate was not melted and non-conformal contact resulted (with relatively weak adhesion expected).

In general, substrate melting can be predicted by estimating the interface temperature between the droplet and substrate. Modeling the droplet and substrate as semi-infinite bodies that are suddenly brought into contact results in the following expression for the interface temperature (ignoring phase change) [21–23].

$$T_{interface} = T_{s,0} + (T_{d,0} - T_{s,0})\frac{1}{1 + e_s/e_d} \quad (4)$$

Here $e_i = \sqrt{(k\rho C_p)_i}$ is the thermal effusivity with thermal conductivity k, density ρ, and heat capacity C_p, $i = d$ for droplet, $i = s$ for substrate, and $T_{s,0}$ and $T_{d,0}$ are the initial temperatures of the substrate and droplet, respectively. For the case of Pt95.5-Ru4.5 printed on an Inconel substrate (Fig. 5b and c), according to Eq. (4), $T_d \geq 1817$C is needed to melt the substrate. Though the precise droplet temperature for this experiment is not known, it is almost certainly greater than this critical temperature given the liquidus temperature of 1795 °C and observation that the particle was fully melted. Thus, it is in line with expectations that substrate melting and conformal contact were achieved. For the case of Pt95.5-Ru4.5 on the same alloy substrate (Fig. 5d and e), the critical droplet temperature needed to achieve substrate melting is 3523 °C. Here, we judge that our experiments did not heat the droplet to this temperature, explaining the poor interface observed in cross-section. Importantly, this analysis ignores the contact thermal resistance effect due to any surface impurities or surface roughness, which will likely have some effect due to additional thermal resistance and

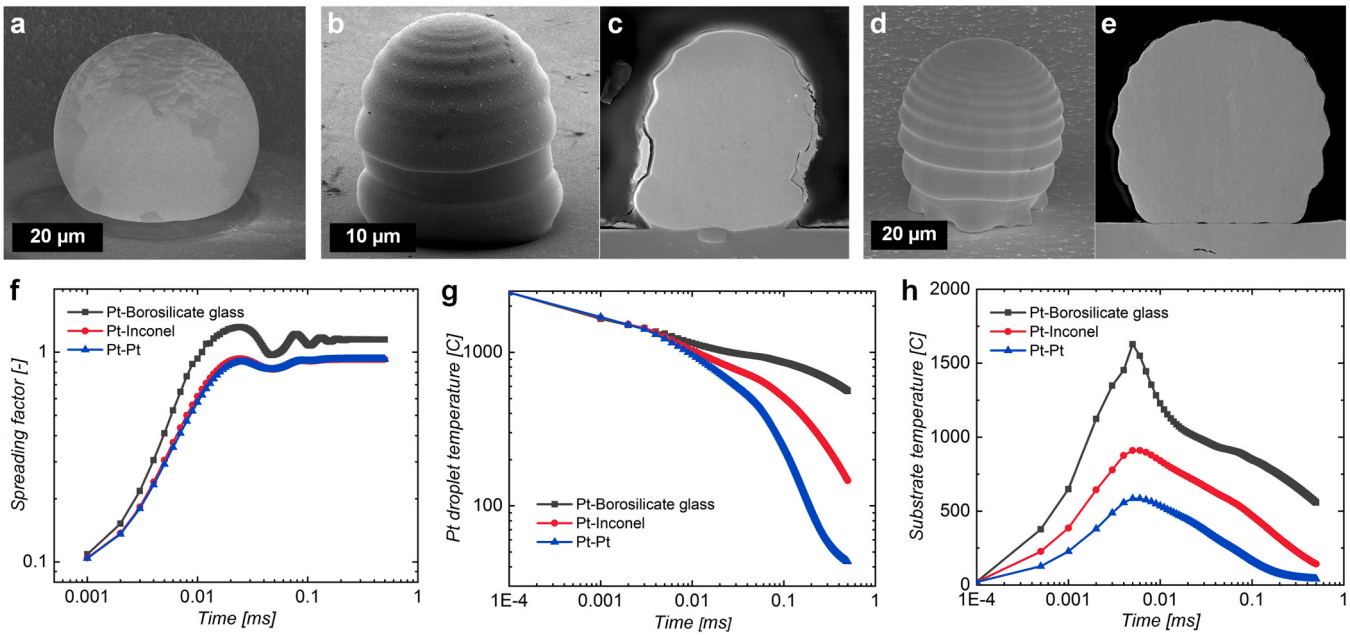

Fig. 5. Printing of Pt95.5-Ru4.5 on various substrates and results of finite element analysis of droplet impact, spreading, and solidification. Exemplary SEM images of Pt95.5-Ru4.5 particles printed on (a) borosilicate glass, (b and c) Inconel 625, and (d and e) Pt95.2-Ru4.8. (c) is a polished cross-section of the particle in image (b), showing conformal contact and metallurgical bonding between the droplet and substrate at the interface. (e) is a polished cross-section of the particle in image (d), showing non-conformal contact and no visible metallurgical bonding. (f) Simulated spreading factor evolution of a molten platinum particle printed on these substrates. (g) Simulated cooling curves of printed platinum particles. (h) Temperature profiles of the substrate impact center corresponding to (g).

modification of the contact area. It is possible to improve the interface temperature estimation from Eq. (4) by accounting for phase change of either material, but it is shown in [23] that this does not significantly change the resulting interface temperature in most cases. In particular, consideration of phase change does not affect the critical temperature thresholds that determine whether the droplet initially remains molten and whether the substrate will melt.

3.4. Morphology of solidified droplets

The different substrates used in the examples shown in Fig. 5a–e also highlight different possible solidified droplet morphologies. For Inconel 625 and Pt95.2-Ru4.8 substrates, ripples are visible in the surface of the solidified morphology. This can result when the timescale of solidification is comparable to the timescale of damping within the droplet. The ripple pattern represents the inertial-capillary oscillations solidified in place by the moving droplet solidification front. If the cooling rate is much smaller than the rate of viscous energy dissipation, the oscillations are dampened via viscous dissipation as the droplet cools. The timescales of oscillation (t_{osc}) and viscous damping (t_{damp}) are as follows for the case of a low Weber number [21].

$$t_{osc} \approx 2.3\sqrt{\rho R^3/\sigma} \tag{5}$$

$$t_{damp} \approx 0.035\frac{R^2}{v} \tag{6}$$

Here, R is the droplet radius, ρ is the density, σ is the surface tension, and v is the kinematic viscosity. The solidification time for the droplet is estimated as [21]

$$t_{sol} \approx \frac{R^2\rho C_s}{k}\left[\frac{1}{St}+\beta\right] \tag{7}$$

where C_s is the droplet heat capacity and k is the thermal conductivity of either the droplet or the substrate, depending on which is lower and thus limiting. St is the Stefan number, $St = \frac{C_p(T_{melt}-T_s)}{\Delta H_f}$, where T_{melt} is the particle melting point, T_s is the substrate temperature and ΔH_f is the latent heat of fusion. β accounts for droplet overheat, $\beta = \frac{T_d-T_s}{T_{melt}-T_s}$, where T_d is the maximum droplet temperature.

Taking $T_d = 2500$ °C, we compare the timescales of oscillation, damping, and solidification for the cases shown in Fig. 5. For these estimates the droplet diameters are measured from each SEM image and the thermal conductivities (in W/m-K) used are as $k_{glass} = 1, k_{Inconel} = 10$, and $k_{Pt-Ru} = 70$. For Fig. 5a (borosilicate glass substrate), t_{osc} and t_{damp} are both ~10–100 μs, while t_{sol} is ~1000 μs; thus we expect that ripples will be small and only be visible near the contact line. For Fig. 5b–e (Inconel 625 substrate and Pt-Ru substrate), t_{osc}, t_{damp} and t_{sol} are ~10 μs for all cases and therefore it is expected that the ripples freeze before they may be damped, as is seen in the images. Simulation results reveal similar ripple patterns.

We have additionally studied the droplet-substrate impingement and solidification processes using finite element analysis (FEA, details in SI). As presented in Fig. 5f, the FEA predicts that a molten Pt droplet (2250 °C, D = 50 μm) will spread and recoil freely on a borosilicate glass substrate before it fully solidifies. On the other hand, when impacting on an Inconel or Pt substrate, the solidification time of Pt is comparable to its oscillation/damping time due to faster heat transfer. As a result, Pt solidifies with less spreading and surface ripples are more significant. In Fig. 5g and h we show the average droplet temperature and substrate impact center temperature versus time, as calculated by the FEA, for Pt-Ru on the three substrates. Solidification on borosilicate glass is slowest due to the substrate's low thermal effusivity, yet the substrate surpasses its softening temperature (820 °C) while the droplet cools.

4. Discussion

Metals are particularly suited for DPEM due to their high thermal conductivities as compared with polymers and ceramics, which in general make it possible to deliver sufficient energy to melt the particles in-flight without excessive overheating of the particle surface. Here, we demonstrated DPEM printing for limiting cases of low and high melting point metals, and its compatibility with various substrates. Notably, in

particular cases, DPEM enabled metallurgical bonding between deposited droplets and the substrate, droplet-to-droplet bonding and conformity with no porosity, and metal-glass adhesion. Further, DPEM introduces the opportunity to control the temperature of each individual droplet independent of the substrate temperature. This is an important capability for controlling metallurgy and will likely be necessary to manage heat accumulation and retain dimensional accuracy during printing. DPEM can also be extended to a wide range of printing materials, for example gold, silver or copper for electrical applications, or titanium for structural applications. With these and other materials, viability may depend on factors such as the availability of lasers with appropriate power and wavelength, atmosphere control requirements, and particle feedstock availability. To achieve the precision required for high-quality printing, factors such as the electric field configuration, field focusing effects, and charge accumulation (for non-conductive substrates) will need to be considered. The optical configuration may also influence the precision, for example a symmetric configuration that enables heating from all sides may be advantageous in avoiding particle trajectory alteration. Last, in an effort to enable continuous on-demand printing, a current effort is aimed at understanding how to provide particles continuously to the meniscus and what the limiting printing rate is for a given configuration.

5. Conclusion

We presented a high-resolution direct metal printing method (DPEM) wherein molten metal droplets are deposited on-demand from a nozzle without requiring contact between the molten metal and a reservoir or orifice material. DPEM's unique combination of capabilities is likely to be valuable for applications where direct printing of high-resolution bulk metal features is needed. These include highly detailed medical implants and surgical instruments as well as decoration of polymer- and ceramic-based implants with radiopaque markers; RF electronics with high-conductivity traces; and features in jewelry and watches that simplify labor-intensive manufacturing processes or enable more complex designs. Continued development of DPEM to achieve continuous and/or high-frequency on-demand particle ejection, as well as further understanding of trajectory control and particle-substrate interaction is necessary to realize a commercially viable technology.

CRediT authorship contribution statement

J.D.B. and A.J.H. conceived of the research topic. H.M., J.D.B., U.P. M. and A.J.H. planned and designed the experiments. H.M. designed and fabricated the experimental apparatus and performed the experiments, characterization, microscopy and related analyses. K.Z. conducted the numerical simulations. All authors discussed the results, and jointly wrote and revised the manuscript.

Declaration of Competing Interest

The authors declare the following financial interests/personal relationships which may be considered as potential competing interests: A. J.H., J.D.B. and H.M. are co-inventors on a patent application related to this work. The authors have no other competing interests.

Acknowledgements

Financial support was provided by BAE Systems Inc. and the MIT Deshpande Center for Technical Innovation. We thank Jiyun Kang and Shaymus Hudson for assistance with characterization, in particular cross-sectioning samples, polishing, etching, and optical and electron microscopy; and Prof. Cem Tasan for helpful discussions. We also thank Ryan Penny for input and guidance in the areas of optics and lasers; and Dan Gilbert, Paul Carson and Joe Wight for their assistance with machining and fabrication in the Mechanical Engineering Manufacturing Shop at MIT. This work made use of the MRSEC Shared Experimental Facilities at MIT, supported by the National Science Foundation under award number DMR-1419807.

Author contributions

J.D.B. and A.J.H. conceived of the research topic. H.M., J.D.B., U.P. M. and A.J.H. planned and designed the experiments. H.M. designed and fabricated the experimental apparatus and performed the experiments, characterization, microscopy and related analyses. K.Z. conducted the numerical simulations. All authors discussed the results, and jointly wrote and revised the manuscript.

Data availability

The data generated and analyzed during the current study are available from the corresponding author on reasonable request.

Appendix A. Supporting information

Supplementary data associated with this article can be found in the online version at doi: 10.1016/j.addma.2020.101703.

References

[1] C. Meier, R.W. Penny, Y. Zou, J.S. Gibbs, A. Hart. Thermophysical Phenomena in Metal Additive Manufacturing by Selective Laser Melting: Fundamentals, Modeling, Simulation and Experimentation 2017.
[2] J. Scott, N. Gupta, C. Weber, S. Newsome, T. Wohlers, T. Caffrey, Additive Manufacturing: Status and Opportunities, IDA, Science and Technology Policy Institute,, Washington, DC, 2012.
[3] C.Y. Yap, C.K. Chua, Z.L. Dong, Z.H. Liu, D.Q. Zhang, L.E. Loh, S.L. Sing, Review of selective laser melting: materials and applications, Appl. Phys. Rev. 2 (4) (2015), 041101.
[4] P.K. Gokuldoss, S. Kolla, J. Eckert, Additive manufacturing processes: selective laser melting, electron beam melting and binder jetting: selection guidelines, Materials 10 (6) (2017) 672.
[5] W.E. Frazier, Metal additive manufacturing: a review, J. Mater. Eng. Perform. 23 (6) (2014) 1917–1928.
[6] A. Kamyshny, J. Steinke, S. Magdassi, Metal-based inkjet inks for printed electronics, Open Appl. Phys. J. 4 (1) (2011).
[7] J.M. Hoey, A. Lutfurakhmanov, D.L. Schulz, I.S. Akhatov, A review on aerosol-based direct-write and its applications for microelectronics, J. Nanotechnol. 2012 (2012).
[8] B.W. An, K. Kim, H. Lee, S.Y. Kim, Y. Shim, D.Y. Lee, J.Y. Song, J.U. Park, High-resolution printing of 3D structures using an electrohydrodynamic inkjet with multiple functional inks, Adv. Mater. 27 (2015) 4322–4328.
[9] A. Khan, K. Rahman, D.S. Kim, K.H. Choi, Direct printing of copper conductive micro-tracks by multi-nozzle electrohydrodynamic inkjet printing process, J. Mater. Process. Technol. 212 (2012) 700–706.
[10] B. Zhang, B. Seong, J. Lee, V. Nguyen, D. Cho, D. Byun, One-step sub-micrometer-scale electrohydrodynamic inkjet three-dimensional printing technique with spontaneous nanoscale joule heating, ACS Appl. Mater. Interfaces 9 (2017) 29965–29972.
[11] M.E. Orme, E.P. Muntz. U.S. Patent 5,171,360, Method Droplet Stream Manufacturing 1992.U.S. Patent 5,171,360.
[12] J.-H. Chun, C.H. Passow, N.P. Suh, Droplet-based manufacturing, CIRP Ann. 42 (1) (1993) 235–238.
[13] J.W. Priest, C. Smith, P. DuBoisLiquid Metal Jetting for Printing Metal Parts, In: Proceedings of the Solid Freeform Fabrication, University of Texas at Austin, *TX*, pp. 1–10, 1997.
[14] T. Metz, G. Birkle, R. Zengerle, P. Koltay. StarJet: Pneumatic Dispensing of Nano- to Picoliter Droplets of Liquid Metal, In: Proceedings of the IEEE International Conference on Micro Electro Mechanical Systems (MEMS) 2009 43 46.
[15] M. Suter, E. Weingärtner, K. Wegener, MHD printhead for additive manufacturing of metals, Procedia CIRP 2 (2012) 102–106.
[16] M. Orme, R.F. Smith, Enhanced aluminum properties by means of precise droplet deposition, J. Manuf. Sci. Eng. 122 (3) (2000) 484–493.
[17] I. Karampelas, S. Vader, Z. Vader, V. Sukhotskiy, A. Verma, G. Garg, M. Tong, E. Furlani. Drop-on-Demand 3D Metal Printing TechConnect briefs 2017.
[18] Q. Liu, M. Orme, High precision solder droplet printing technology and the state-of-the-art, J. Mater. Process. Technol. 115 (3) (2001) 271–283.
[19] M. Michaelis, J. Zhu, M. Orme. Heat Transfer Manipulation Precision Droplet Manufacturing: Simulation Exp. 2002.
[20] P. Fima, T. Gancarz, J. Pstrus, K. Bukat, J. Sitek, Thermophysical properties and wetting behavior on cu of selected sac alloys, Solder. Surf. Mt. Technol. 24 (2) (2012) 71–76.

[21] S. Schiaffino, A.A. Sonin, Molten droplet deposition and solidification at low Weber numbers, Phys. Fluids 9 (11) (1997) 3172–3187.
[22] H.S. Carslaw, J.C. Jaeger, Conduction of Heat in Solids, Oxford Univ. Press,, 1986.
[23] J. de Ruiter, D. Soto, K.K. Varanasi, Self-peeling of impacting droplets, Nat. Phys. 14 (1) (2018) 35.
[24] A.J. Hart, J. Beroz, H. Maghsoodi, Discrete deposition of particles, U.S. Patent 9,937,522 (2015).